Online Prediction of Battery Discharge and Estimation of Parasitic Loads for an Electric Aircraft

Brian Bole[1], Matthew Daigle[2], George Gorospe[1]

[1] *SGT, Inc., NASA Ames Research Center, Moffett Field, CA 94035*
brian.bole@nasa.gov, george.gorospe@nasa.gov

[2] *NASA Ames Research Center, Moffett Field, CA 94035*
matthew.j.daigle@nasa.gov

Abstract

Predicting whether or not vehicle batteries contain sufficient charge to support operations over the remainder of a given flight plan is critical for electric aircraft. This paper describes an approach for identifying upper and lower uncertainty bounds on predictions that aircraft batteries will continue to meet output power and voltage requirements over the remainder of a flight plan. Battery discharge prediction is considered here in terms of the following components; (i) online battery state of charge estimation; (ii) prediction of future battery power demand as a function of an aircraft flight plan; (iii) online estimation of additional parasitic battery loads; and finally, (iv) estimation of flight plan safety. Substantial uncertainty is considered to be an irremovable part of the battery discharge prediction problem. However, high-confidence estimates of flight plan safety or lack of safety are shown to be generated from even highly uncertain prognostic predictions.

1. Introduction

Electric propulsion can provide a number of advantages over combustion powered vehicles, such as reduced noise, zero emissions, more responsive control of output power, reduced part count, and reduced weight. In such vehicles, it is critical to monitor battery charge and to estimate the ability of the battery to support flight activities as it is discharged.

As is the case with many applications of prognostics, unavoidable uncertainties or inaccuracies in system state estimates, system dynamics modeling, and future input estimation will complicate the prediction problem (Sankararaman & Goebel, 2013). The presence of substantial uncertainty in prognostic estimates however does not necessarily rule out

its usefulness to a decision maker. If prognostic uncertainty can be represented by a probability distribution or bounded by a confidence interval, than it may still be extremely useful for evaluating the potential risk and reward of various control options (Edwards et al., 2010).

The battery discharge prognostic algorithm described in this paper uses three primary tools to manage prognostic uncertainty. First, unscented Kalman filtering (UKF) is used to update probabilistic estimates of internal battery states, based on a series of battery current and voltage observations. Second, a predefined flight plan is used to identify upper and lower uncertainty bounds around future system loading demands. Finally, uncertainty is propagated over a prognostic horizon to identify uncertainty bounds on prognostic estimates.

This paper extends our previous work on battery discharge prediction for electric vehicles. The battery modeling and UKF state estimation approaches explained here were recently published in (Quach et al., 2013). The aerodynamic and aircraft powertrain models used here to estimate future battery power demand as a function of a flight plan were recently published in (Bole et al., 2013). Our previous work considered the prediction of remaining flying time given a flight plan with no fixed termination time. That approach is supplemented here by introducing new prognostic metrics that will be used to evaluate the feasibility of completing a fixed duration mission. This paper also describes the incorporation of parasitic resistance faults into prognostic predictions.

This paper is organized as follows. The prototype electric aircraft used to demonstrate battery charge estimation and discharge prediction techniques is described in Section 2. Estimation of battery SOC using unscented Kalman filtering and an equivalent circuit model is presented in Section 3. Battery demand modeling as a function of airspeed, acceleration, and angle of climb is described in Section 4. The online detection of parasitic battery loads is described in Section 5. Mission

Figure 1. Edge-540T during landing

Figure 2. Motor System Diagram

feasibility prediction and battery SOC estimation at the end of a flight plan is presented in Section 6. Experimental results are described in Section 7. Finally, concluding remarks are given in Section 8.

2. PROTOTYPE ELECTRIC VEHICLE BACKGROUND

Battery discharge prognosis is analyzed here in the context of a prototype battery powered aircraft. The prototype aircraft is a 33% scaled Edge-540T, with electric propulsion, shown in Fig. 1. It is 98 inches long, with a 100 inch wing span, 1881 in^2 of wing area, and weighs 47.4 lbs. This aircraft is operated by researchers at the NASA Langley Research center, and has been the subject of several publications on battery discharge prediction and prognostics-based decision making (Saha et al., 2011, 2012; Balaban & Alonso, 2013).

The aircraft powertrain is illustrated in Fig. 2. The propeller of the UAV is driven by two tandem mounted outrunner brushless DC motors that are each powered by a series connection of two lithium polymer battery packs. Each of the battery packs consist of five series connections of two 3900mAh lithium polymer pouch cells wired in parallel. The total rated capacity of each pack is 7800 mAh with a 50 C max burst discharge. When fully charged, each 5-cell pack has an open circuit voltage of 21 V (4.2 V per cell).

Power flow from the battery packs to the driving motors is controlled by a Jeti 90 Pro Opto electric speed controller (ESC). The ESC sends synchronized voltages to the propeller motors at a duty cycle determined by a throttle input, which is either sent by remote control from a pilot or by an onboard autopilot.

Inductive loop current sensors are mounted on the positive lead feeding each ESC. Additional current sensors are also mounted on the positive feed from each of the four batteries. The positive lead of each battery is also tapped to provide the data system with battery voltage measurements. These are the signals that online battery discharge prognostic algo-

rithms will use to estimate battery SOC and to predict SOC at end of mission.
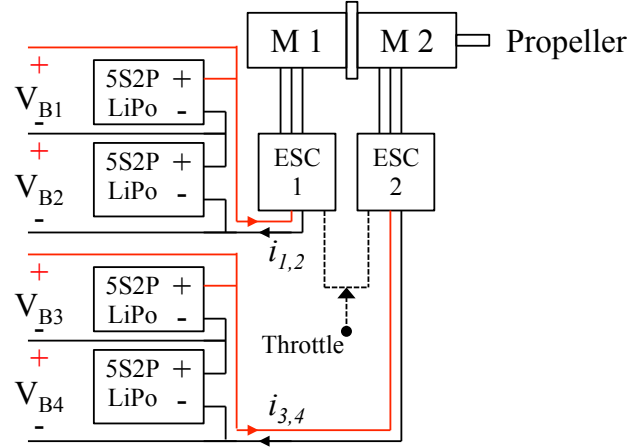
3. BATTERY MODELING

The equivalent circuit model shown in Fig. 3 is used to replicate battery current and voltage dynamics as a function of estimated battery state of charge (SOC). This battery model contains six electrical components that are tuned to recreate the observed current-voltage dynamics of the Edge-540T battery packs. Battery charge is stored in the equivalent circuit model capacitor, C_b. The R_s, C_s and R_{cp}, C_{cp} circuit element pairs are used to capture standard battery phenomenon, such as internal resistance drops and hysteresis effects.

Because the equivalent circuit model is used to model the input-output response of a battery rather than its internal electrochemical states, the number of electrical components used, and there arrangement within an equivalent circuit can vary widely in application (Chen & Rincon-Mora, 2006). Additionally, because battery input-output dynamics are known to change as a function of internal battery charge, is often the case that some of the parameters in an equivalent circuit model are parameterized as functions of battery state of charge (SOC) (Zhang & Chow, 2010). There is no universal guidance on how equivalent circuit parameters should be varied as functions of SOC, and many differing approaches are seen in literature. It was decided based on qualitative observation that defining C_b, C_{cp}, and R_{cp} as parameterized functions of battery SOC gave an acceptable trade-off between the number of parameters to be identified and model error.

The following SOC parameterizations were used for the C_b, C_{cp}, and R_{cp} parameters in Fig. 3:

$$C_b = C_{Cb0} + C_{Cb1} \cdot \text{SOC} + C_{Cb2} \cdot \text{SOC}^2 + C_{Cb3} \cdot \text{SOC}^3 \quad (1)$$

$$C_{cp} = C_{cp0} + C_{cp1} \cdot \exp\left(C_{cp2}\left(\text{SOC}\right)\right) \quad (2)$$

2
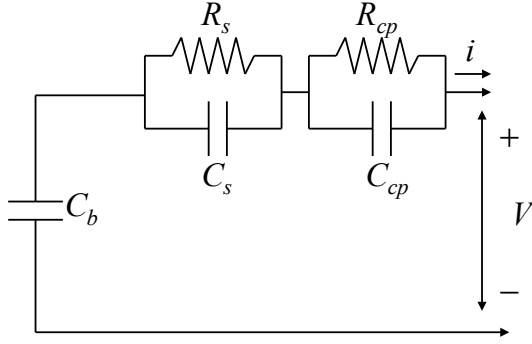
Figure 3. Equivalent circuit battery model.

$$R_{cp} = R_{cp0} + R_{cp1} \cdot \exp\left(R_{cp2}\left(\text{SOC}\right)\right) \qquad (3)$$

where the coefficients in the parameterized models for C_b, C_{cp}, and R_{cp} must be tuned based on observed current-voltage battery data over a range of battery SOC values.

Battery SOC is defined here as:

$$\text{SOC} = 1 - \frac{q_{max} - q_b}{C_{max}} \qquad (4)$$

where q_b represents the charge stored in C_b, q_{max} is the maximum charge that the battery can hold, and C_{max} is the maximum charge that can be drawn from the battery. Note that, the maximum charge that can be drawn from the battery will be lower than the amount of charge stored in the battery due to electrochemical side-reactions that lock some portion of charge carriers in the battery. The term coulombic efficiency is used to refer to the portion of stored charge that is recoverable during the discharge of the battery. There are some mechanisms including resting the battery that can unlock some of its lost capacity, however, the overall trend is inevitably downward.

Two laboratory experiments were used to fit all of the parameters in the equivalent circuit model to the lithium polymer packs used on the Edge-540T. Adapting the equivalent circuit model to account for manufacturing variation and differences in battery state-of-health is performed by varying only the battery charge storage capacity term, q_{max}, and the series resistance term, R_s, in equivalent circuit model. All other fitted parameters in the equivalent circuit model are unvaried across all Edge-540T packs. The q_{max} and R_s terms are identified by running separate characterization cycles for each battery pack prior to flight testing. A sample implementation for the online adaptation of these parameters to track age-dependent changes in battery dynamics is found in (Bole et al., 2014).

Examples of measured and modeled battery voltage curves for two laboratory characterization cycles are shown in Figs. 4 and 5. The results shown in Fig. 4 demonstrate a characterization experiment in which a battery is discharged at a low current from a fully charged state. During this low cur-
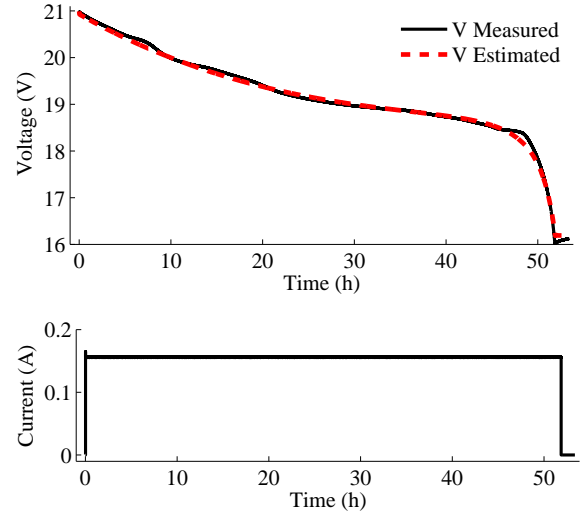
Figure 4. Comparison between measured and predicted battery voltage over a low current discharge.
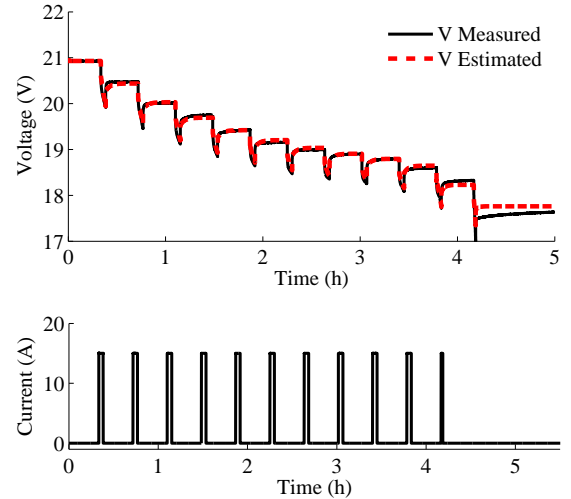
Figure 5. Comparison between measured and predicted battery voltage over a pulsed current discharge.

rent discharge test, the voltage across the C_b capacitor plays a dominate role. Thus, this experiment allows the C_b parameters in the equivalent circuit model to be fit in isolation.

Fig. 5 shows sample results from a second characterization experiment in which a battery is discharged using a series of current pulses. This experiment exposes voltage dynamics that must be fit by the R_s, C_s, C_{cp} and R_{cp} parameters in the equivalent circuit model.

3.1. Battery State Estimation

The identified battery model can then be used to implement an observer for the internal battery states based on sampled voltage and current data. The observer will attempt to estimate the internal states of each of the capacitors (C_b, C_s, and C_{cp}) in the equivalent circuit model.

The unscented Kalman filter (UKF) (Julier & Uhlmann, 1997, 2004) is a flexible tool for computing probabilistic belief in system state estimates based on stochastic (and possibly nonlinear) models of system dynamics. The UKF assumes a general nonlinear form of the state and output equations, and efficiently propagates model and state uncertainties without the need to calculate Jacobians (unlike the extended Kalman filter). The UKF is restricted to additive Gaussian noise random processes; however use of the unscented transform, a deterministic sampling method, allows random variables with non-Gaussian distributions to be incorporated using a minimal set of weighted samples, called *sigma points* (Julier & Uhlmann, 1997).

The UKF takes as inputs the system inputs, $\mathbf{u}(k)$, and the measured system outputs, $\mathbf{y}(k)$. The UKF gives as output, performing estimation using the battery model, a probability distribution for the state, $p(\mathbf{x}(k)|\mathbf{y}(0:k))$, described in the form of weighted sigma points $(\mathcal{X}, \mathbf{w})$. From the sigma points, estimates of SOC, and voltage can be directly derived to obtain probability distributions of these quantities.

The number of sigma points needed is linear in the dimension of the random variable, and so the statistics of the transformed random variable, i.e., mean and covariance, can be computed much more efficiently than by random sampling (Daigle et al., 2012). Readers interested in the application of UKF and UT to the estimation of battery SOC are referred to our previous papers (Bole et al., 2013; Daigle et al., 2012) and the references therein. Here, it is sufficient to say that model based filtering approaches such as UKF will be much less susceptible to initialization and measurement errors than the Coulomb counting method currently used in many battery monitoring systems (Dai et al., 2006).

4. FUTURE MOTOR POWER DEMAND MODELING

The characterization of net battery power required by aircraft motors over a given set of maneuvers was recently described in (Bole et al., 2013). The powertrain load estimation modeling introduced in (Bole et al., 2013) made use of a set of relatively simple aerodynamics and powertrain dynamics equations that will be recreated here.

The equations presented here make use of the following assumptions: (i) the propeller is mounted on the aircraft nose; (ii) the angle between the thrust vector generated by the propeller and the velocity vector of the aircraft is small; and (iii) aircraft turning forces are small in comparison to the thrust and drag forces on the aircraft in its direction of travel.

Given these assumptions, the sum of the forces acting in the aircraft direction of travel can be expressed as:

$$T_{x_w} = D(v) + m \cdot g \cdot \sin(\alpha) + m \cdot \dot{v} \qquad (5)$$

where T_{x_w} represents the thrust produced by the aircraft in the direction of travel, D represents the drag force acting in the opposite direction of aircraft motion, v represents the aircraft airspeed in units of meters/second, $\dot{v}$ represents acceleration, α represents angle of climb in units of radians, m represents the vehicle mass, and g represents the earth's gravity.

The drag force on the airframe was fitted to the following polynomial function of airspeed and angle of climb,

$$D(v, \gamma) = c_1 + c_2 \cdot v + c_3 \cdot v^2 + c_4 \cdot \alpha$$
$$\text{for } v \geq 15\text{m/s} \qquad (6)$$

During take-off and landing maneuvers when the aircraft speed is less than $15m/s$ the drag force is approximated as $D = 3 \cdot v$. The fitted parameter values used here are: $c_1 = 53.9$, $c_2 = -2.4$, $c_3 = 0.07$, $c_4 = 0.56$

The product of thrust and airspeed gives the motive power exerted by the aircraft on its environment,

$$P_p = \frac{1}{\eta_p} \cdot T_{x_w} \cdot v \qquad (7)$$

where P_p represents propeller output power and η_p represents the approximate propeller output power conversion efficiency. The fitted value $\eta_p = 0.7652$ was found using a commercial aerodynamics simulator.

A fixed power conversion efficiency is assumed here for the aircraft motors and other power electronics,

$$P_{ESC} = \eta_e \cdot P_p \qquad (8)$$

where η_e represents a power conversion efficiency factor and P_{ESC} represents net power at the input to the aircraft's two ESCs. The average efficiency of aircraft motors and power electronics was estimated here to be about 85%, $\eta_p = 0.85$.

The net ESC input power is equal to the sum of the power outputs from the two series connected battery strings,

$$P_{ESC} = P_{B1,2} + P_{B3,4} \qquad (9)$$

where $P_{B1,2}$ and $P_{B3,4}$ represent the battery power output for batteries B1,B2 and B3,B4 as denoted in Fig. 2.

Although both ESCs receive the same throttle input command, their individual power draw is known to have a proportional relationship.

$$P_{B1,2} = \lambda \cdot P_{B3,4} \qquad (10)$$

where λ is constant of proportionality. This constant λ was estimated to be about 1.37 over typical use cases for the Edge-540T powertrain.

Substitution of Eqs. (5) - (8) yields an expression for the approximate ESC input power required to fly at a particular airspeed and angle of climb,

$$P_{ESC} = \frac{1}{\eta_e \eta_p} \cdot T_{x_w} \cdot v$$
$$= \frac{v}{\eta_e \eta_p} \cdot \left(D\left(v, \alpha\right) + mg \cdot \sin\left(\alpha\right) + m\dot{v} \right) \quad (11)$$

The power demands on battery strings $B_{1,2}$ and $B_{3,4}$ are then estimated as,

$$P_{B_{1,2}} = \frac{\lambda}{1 + \lambda} \cdot P_{ESC}$$
$$P_{B_{3,4}} = \frac{1}{1 + \lambda} \cdot P_{ESC} \quad (12)$$

4.1. Uncertainty Representation

Uncertainty in future powertrain loading demands are considered here to be unavoidable in environmental and system dynamics modeling. Uncertainty in future load prediction is represented here by defining a median future demand prediction with an upper and lower uncertainty bound.

Fig. 6 shows predicted and measured battery output power and battery output energy respectively for the battery string B1,B2 over a sample flight of the Edge-540T. The upper and lower uncertainty bounds shown in Fig. 6 represent $\pm 30\%$ deviation from the future battery power estimated using Eqns. (11) and (12) with the following sample flight plan.

1. Takeoff and climb to ∼200 meters (duration = 60 s) ($\alpha = 2.8°$, $v_0 = 0\frac{m}{s}$, $\dot{v} = 0.4\frac{m}{s^2}$)

2. Maintain altitude and approximate airspeed of $v = 23\frac{m}{s}$ (duration = 265 s) ($\alpha = 0°$, $v = 23\frac{m}{s}$, $\dot{v} = 0\frac{m}{s^2}$)

3. Maintain altitude and approximate airspeed of $v = 29\frac{m}{s}$ (duration = 225 s) ($\alpha = 0°$, $v = 29\frac{m}{s}$, $\dot{v} = 0\frac{m}{s^2}$)

4. Maintain altitude and approximate airspeed of $v = 22\frac{m}{s}$ (duration = 140 s) ($\alpha = 0°$, $v = 22\frac{m}{s}$, $\dot{v} = 0\frac{m}{s^2}$)

5. Land aircraft (duration = 120 s) ($\alpha = -3°$, $v_0 = 22\frac{m}{s}$, $\dot{v} = -0.18\frac{m}{s^2}$)

It can be seen from Fig. 6 that the actual battery power does not always fall within the plotted upper and lower uncertainty bounds. Notably the battery loads during the takeoff and climb portion of the flight plan (from 0-60 seconds) are seen to exceed the maximum predicted power at some points. Also, the battery loads during landing maneuver (from 690-810 seconds) are seen to exceed the minimum and maximum predicted power. The exceedances seen in takeoff and landing maneuvers are due to unmodeled transient dynamics in the system. These transients are short lived however, and the
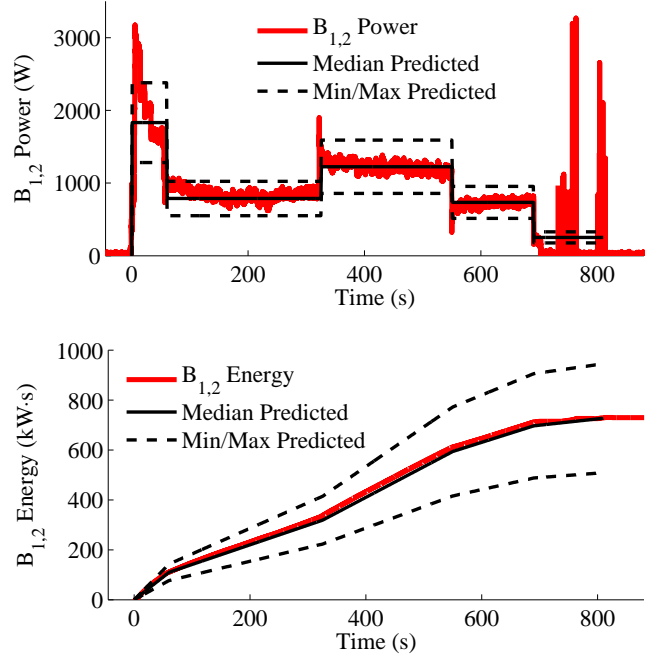
Figure 6. Plots of measured and predicted $B_{1,2}$ output power and energy over a sample flight.

measured battery energy consumed over the sample flight is seen to fall well within the estimated uncertainty bounds.

5. PARASITIC LOAD ESTIMATION

A potential fault mode for the Edge aircraft is some fault in the electrical power system that manifests as a parasitic load on the batteries. Because this fault mode presents an increased load on the batteries, it will have effect of increasing the battery charge required to complete a flight plan. Future battery load estimates and battery discharge prediction would thus be biased if the parasitic load faults were not incorporated. In such a situation, an integrated diagnostics and prognostics approach is required (Bregon, Daigle, & Roychoudhury, 2012).

In our case, we consider a parasitic resistance that is located in parallel with the batteries. The parasitic current, i_p, is the difference between the total battery current, i, and the current going to the motors, i_m. In the aircraft, both i and i_m are measured as well as the total battery voltage V.

A residual, defined as the difference between an observed signal and its model-predicted value, can be defined for the parasitic fault detection based on the measured values of i and i_m. In the nominal case, our model for i is $i = i_m$. We can then define a residual, r_i, as $r = i^* - i_m^*$, where the * superscript indicates a measured value. Nominally, $r_i = 0$, and we can define a simple threshold-based fault detector that

triggers when $r_i > T$ for some threshold T. More complex fault detection methods can also be used, e.g., (Daigle et al., 2010). Once a fault is detected, we can estimate the parasitic current at time k using

$$\hat{i}_p(k) = i^*(k) - i_m^*(k), \tag{13}$$

The parasitic resistance can then be estimated using

$$\hat{R}_p(k) = \frac{V_b^*(k)}{\hat{i}_p(k)}. \tag{14}$$

The estimate $\hat{R}_p(k)$ will be noisy, since it is computed based on measured values. Assuming that R_p is constant, we take the median of all computed values to provide a robust estimate of R_p, i.e.,

$$R_p(k) = \text{median}(\{\hat{R}_p(k_j) : k_d \geq k_j \geq k\}), \tag{15}$$

where k_d is the time of fault detection (and the time that fault identification begins).

Since we are only interested in diagnosing the parasitic load fault, the diagnosis approach can be very simple. In general, one may also be concerned with sensor faults, in which case a more complex diagnosis approach is required, e.g., (Balaban et al., 2013; Daigle, Bregon, & Roychoudhury, 2011). In such an approach, additional information must be used to improve the analytical redundancy required for diagnosis.

Experimental results are shown in Figs. 7(a) and 7(b). In the nominal case, parasitic current is estimated to be approximately zero, which is correct for the no fault case. For the fault cases, parasitic current is clearly observed, and parasitic resistances can be estimated. In this data, sensor noise is very low and so the results are very accurate. Additional sensor noise will have a significant impact on the computation of parasitic resistance. Fig. 8 shows the difference in results for additional noise. With higher noise, accuracy reduces and the estimate takes longer to converge. Because we are using a median, the results are still pretty smooth.

6. PREDICTION

We now consider the problem of predicting whether or not the aircraft batteries contain sufficient charge to complete the remainder of a given flight plan. The aircraft batteries are considered to be no longer able to safely support flight activities when any of the battery pack voltages drop below 17V. A 17V pack output voltage corresponds individual lithium-ion cell voltages of approximately 3.4V. Discharging the lithium-ion cells beyond this voltage risks damage or catastrophic failure.

Predictions of the future evolution of battery voltage over a flight plan are generated using estimates of the present battery state, as well as estimates of the future loads to be placed on the battery. As explained in Section 3.1, uncertainty in
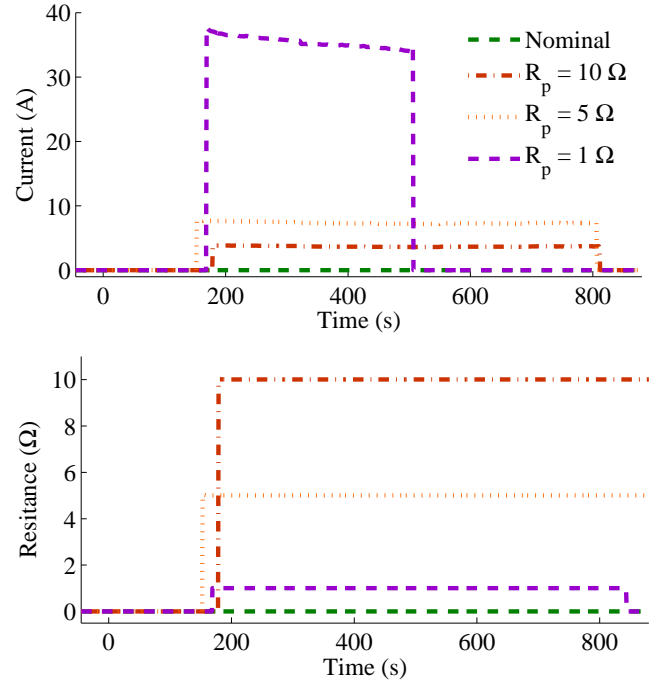
Figure 7. Parasitic current and resistance estimates.
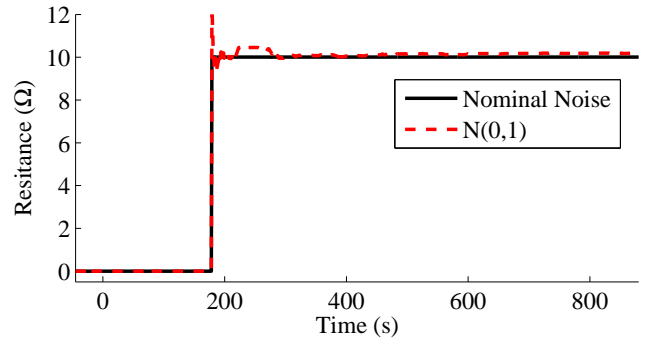
Figure 8. Parasitic resistance estimation with additional sensor noise.

battery state estimates is represented using a weighted set of sigma points. As explained in Section 4.1, uncertainty in predictions of the future battery power to be demanded over the remainder of a flight plan are represented here by upper and lower uncertainty bounds.

The experimental results presented in the next section demonstrate that high confidence assessments on the safety of completing the remainder of a flight plan can be generated by simulating all of the current sigma point state estimates against the extreme upper and lower bounds of anticipated future battery load. If the maximum and minimum sigma points resulting from the application of these future loading extremes are safe, then we must have very high confidence that the mis-

sion will be completed. If some of the simulated sigma points reach a failure state, then we can attempt to further qualify the risk of failure by applying additional analysis techniques.

7. EXPERIMENTAL TESTING OF BATTERY PREDICTION

Fig. 9 shows an electrical schematic for a test stand that is used to simultaneously subject batteries to both a static resistive loads and a dynamic current loads. The B_1 and B_2 batteries shown in Fig. 9 represent two batteries under test. Our test articles are batteries with the same chemistry, capacity, voltage, and manufacturer as the Edge-540T batteries. The i_f component in Fig. 9 represents a dynamic current sink that is programmed to sink the same current as was measured for the $B_{1,2}$ battery chain over a given flight of the Edge-540T. The R_p component in Fig. 9 represents a resistive load that can be switched in parallel with the batteries on command.

A Maccor Series 4000 automated battery cycler is used for the tests described in this section, and for the battery characterization cycling experiments described in Section 3. This programmable test system can be configured to draw or apply static loads or time dependent loads. The testing equipment is capable of sourcing or sinking up to 5kW of power, with current limited to 100A, and voltage limited to 50V. The cycler can be programmed to terminate a loading profile based on current, voltage, or temperature safety thresholds. In the case of the experiments conducted here, a low-voltage safety threshold of 17V per pack was used prevent over discharging the batteries. If this threshold is crossed, the battery loading experiment is terminated immediately and the batteries will be considered failed for the purposes of that simulation run.

Four battery discharge experiments are described here. In all of these experiments the i_f component in Fig. 9 is set equal to a 10 Hz sampling of the $i_{B_{1,2}}$ current as measured over a sample flight of the Edge-540T. One experiment is performed with the R_p branch of Fig. 9 open. The resultant battery voltage response should closely follow the trends seen on batteries B_1 and B_2 in the flight test, because they are being subjected to the same current loads. The addition of a parasitic resistance to the battery circuit is tested in the remaining three discharge experiments. Parasitic resistances are added into the battery circuit at approximately 200 seconds into a replayed flight. The lower the value of parasitic resistance injected, the higher the parasitic current draw on the batteries. The additional current drawn by this parasitic load effectively increases the demand on the battery over a simulated flight, and correspondingly increases the risk that the battery lacks sufficient charge to complete a given flight plan. The parasitic resistance values tested were: $\{R_p = 10\ \Omega, R_p = 5\ \Omega$, and $R_p = 1\ \Omega\}$.

Fig. 10 shows B_1 and B_2 voltage measurements and SOC estimates collected during a sample flight, and during four
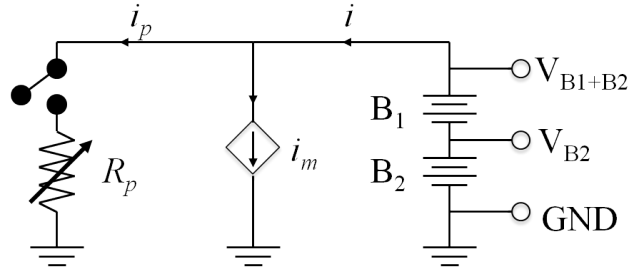
Figure 9. Schematic of battery tester, showing current sources and voltage measurement points.

battery discharge tests conducted in the laboratory. The flight data was collected over an Edge-540T flight that followed the sample flight plan described in Section 4.1. The battery voltage and SOC measurements for the nominal experiment (with no parasitic load injected) are in fact seen to follow the flight measurements. The injection of 10 Ω and 5 Ω parasitic resistances is seen to result in lowered battery voltage and SOC over a sample flight profile. Finally, the injection of a 1 Ω resistance is seen to result in the early termination of the discharge test due to an exceedence of the low-voltage safety threshold at approximately 500 seconds.

Next we consider the generation of prognostic estimates for the aircraft at regular time-indexes over a UAV mission. At each time-index the inputs to the prognostic estimator are (i) a set of sigma points representing battery state estimates; (ii) estimated $\pm30\%$ uncertainty bounds on motor system power demands over a planned set of aircraft maneuvers; and (iii) online estimates of parasitic load faults. Prognostic estimates will be reported in terms of two metrics; (i) the predicted battery SOC at the end of a flight plan, and (ii) the predicted time to reach either the battery low-voltage cut-off threshold or the end of a flight plan.

Fig. 11 shows the evolution of prediction uncertainty bounds for the two prognostic metrics over five battery discharge data sets. The starting uncertainty bounds for the prediction of battery SOC at the end of the flight plan is seen to span from approximately 55% SOC to 10% SOC. The battery EOD estimate is seen to span from approximately 700 seconds to 810 seconds, where 810 seconds marks the expected end of the aircraft flight plan. These uncertainty bounds indicate a predicted worst-case outcome where the batteries reach the low-voltage cut-off threshold at approximately 700 seconds, and a best-case predicted outcome in which the mission will be safely completed.

During the time interval [0,180], all of the worst-case EOD estimates are seen to converge on a belief that the mission will not cause the batteries to fail prior to flight plan completion. This convergence occurs because the battery state evolution observed over the time interval [0,180] turns out to be better that was predicted for the worst-case.
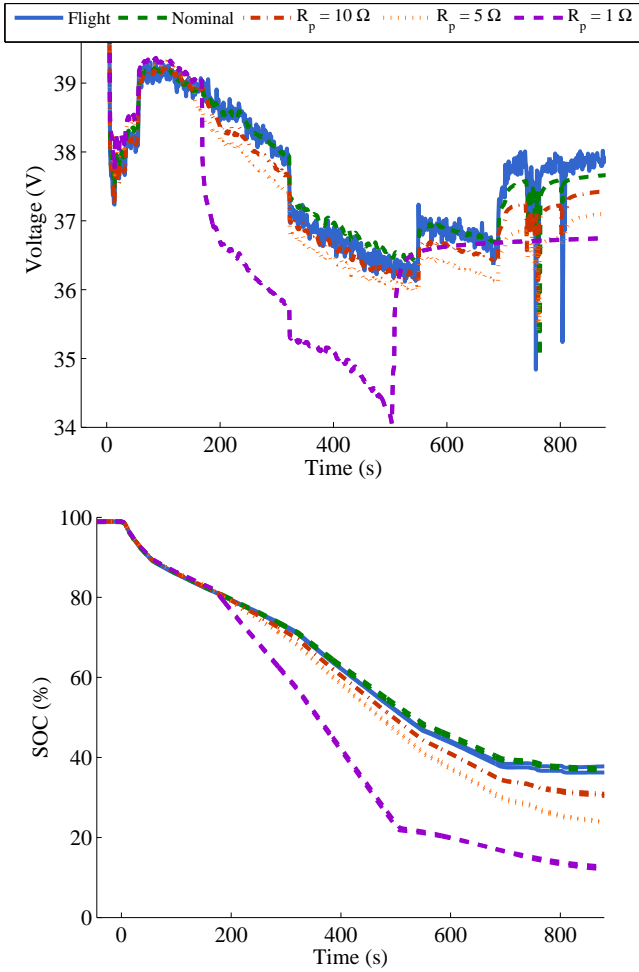
Figure 10. Comparison of voltage measurements (top) and SOC estimates (bottom) for batteries B_1 and B_2 over a sample flight and four test cases that include injected parasitic resistances of various magnitudes.

Figure 11. Prediction uncertainty bounds for two prognostic metrics plotted at 30 second time intervals over five battery discharge data sets. Predicted battery SOC at EOM is shown in the top plot, and predicted time to reach a battery EOD threshold is shown in the bottom plot

Around 200 seconds into the mission a parasitic resistance is injected in parallel with the batteries. The effect that this new parasitic resistance has on predicted future battery loads is clearly seen the predictions of SOC at end of flight plan. For the case of the 1 Ω injected parasitic resistance, predictions of SOC at end of flight plan are seen to rapidly converge to a prediction that the battery charge will be fully depleted prior to the end of the flight plan. The EOD prediction plots show an initial drop in the confidence that batteries will survive the remainder of the flight plan with 5 Ω and 10 Ω of parasitic load. The confidence in flight plan safety for the 5 Ω and 10 Ω cases is then seen to converge to predicting the safe completion of the mission.

This example demonstrates the combination of system state estimation uncertainty and future system load uncertainty into an estimate of prognostic uncertainty. Upper and lower un-

certainty bounds on the space of future outcomes are derived, and the utility of these bounds for making high confidence estimates of flight plan safety is demonstrated. Consideration of situations in which uncertainty bounds indicate that a range of both safe and unsafe evolutions of the system state are possible is identified as a topic for future work. In such situations, knowledge of a probability distribution for the prognostic uncertainty between upper and lower uncertainty bounds, may be needed to quantify the risk and reward of potential supervisory control actions. Extending the prognostic results presented here in this way is possible, but is left as a topic for future work. Flight demonstrations of autonomous and pilot-in-the-loop decision making based on online battery discharge predictions is also planned for future work.

8. CONCLUSIONS

This paper describes an approach for identifying upper and lower uncertainty bounds on predictions that aircraft batteries will continue to meet output power and voltage requirements over the remainder of a flight plan. Uncertainty bounds were generated using uncertain estimates of a battery's state and uncertain predictions of future battery demands. The establishment of upper and lower bounds on prognostic estimates was shown to enable high confidence assessments of amount of safe flying time remaining before there is appreciable risk of the battery output voltage dropping below specified lower limits.

ACKNOWLEDGMENT

REFERENCES

Balaban, E., & Alonso, J. (2013). A modeling framework for prognostic decision making and its application to uav mission planning. In *Annual conference of the prognostics and health management society*.

Balaban, E., Narasimhan, S., Daigle, M., Roychoudhury, I., Sweet, A., Bond, C., & Gorospe, G. (2013). Development of a mobile robot test platform and methods for validation of prognostics-enabled decision making algorithms. *International Journal of Prognostics and Health Management*, *4*(1).

Bole, B., Kulkarni, C. S., & Daigle, M. (2014). Adaptation of an electrochemistry-based li-ion battery model to account for deterioration observed under randomized use. In *Annual conference of the prognostics and health management society*.

Bole, B., Teubert, C., Chi, Q. C., Edward, H., Vazquez, S., Goebel, K., & Vachtsevanos, G. (2013). SIL/HIL replication of electric aircraft powertrain dynamics and inner-loop control for V&V of system health management routines. In *Annual conference of the prognostics and health management society*.

Bregon, A., Daigle, M., & Roychoudhury, I. (2012, September). An integrated framework for model-based distributed diagnosis and prognosis. In *Annual conference of the prognostics and health management society 2012* (p. 416-426).

Chen, M., & Rincon-Mora, G. (2006). Accurate electrical battery model capable of predicting runtime and i-v performance. *IEEE Transactions on Energy Conversion*, *21*(2), 504-511.

Dai, H., Wei, X., & Sun, Z. (2006). Online soc estimation of high-power Lithium-Ion batteries used on HEVs. In *IEEE international conference on vehicular electronics and safety*.

Daigle, M., Bregon, A., & Roychoudhury, I. (2011, Oct). Qualitative Event-based Diagnosis with Possible Conflicts: Case Study on the Third International Diagnostic Competition. In *Proceedings of the 22nd international workshop on principles of diagnosis* (p. 285-292). Murnau, Germany.

Daigle, M., Roychoudhury, I., Biswas, G., Koutsoukos, X., Patterson-Hine, A., & Poll, S. (2010, September). A comprehensive diagnosis methodology for complex hybrid systems: A case study on spacecraft power distribution systems. *IEEE Transactions of Systems, Man, and Cybernetics, Part A*, *4*(5), 917–931.

Daigle, M., Saxena, A., & Goebel, K. (2012). An efficient deterministic approach to model-based prediction uncertainty. In *Annual conference of the prognostics and health management society*.

Edwards, D., Orchard, M., Tang, L., Goebel, K., & Vachtsevanos, G. (2010). Impact of input uncertainty on failure prognostic algorithms: Extending the remaining useful life of nonlinear systems. In *Annual conference of the prognostics and health management society*.

Julier, S. J., & Uhlmann, J. K. (1997). A new extension of the Kalman filter to nonlinear systems. In *Proceedings of the 11th international symposium on aerospace/defense sensing, simulation, and controls* (pp. 182–193).

Julier, S. J., & Uhlmann, J. K. (2004, March). Unscented filtering and nonlinear estimation. *Proceedings of the IEEE*, *92*(3), 401–422.

Quach, C. C., Bole, B., Hogge, E., Vazquez, S., Daigle, M., Celaya, J., & Goebel, K. (2013). Battery charge depletion prediction on an electric aircraft. In *Annual conference of the prognostics and health management society*.

Saha, B., Koshimoto, E., Quach, C. C., Hogge, E. F., Strom, T. H., Hill, B. L., ... Goebel, K. (2011). Battery health management system for electric UAVs. In *IEEE aerospace conference*.

Saha, B., Quach, C. C., & Goebel, K. (2012, March). Optimizing battery life for electric UAVs using a Bayesian framework. In *Proceedings of the 2012 ieee aerospace conference*.

Sankararaman, S., & Goebel, K. (2013). Why is the remaining useful life prediction uncertain? In *Annual conference of the prognostics and health management society*.

Zhang, H., & Chow, M.-Y. (2010). Comprehensive dynamic battery modeling for PHEV applications. In *IEEE power and energy society general meeting*.

BIOGRAPHIES

Brian M. Bole graduated from the FSU-FAMU School of Engineering with a B.S. in Electrical and Computer Engineering and a B.S. in Applied Math. Brian received M.S. and Ph.D. degrees in Electrical Engineering from the Georgia Institute of Technology. His research interests include: analysis of stochastic processes, risk analysis, and optimization of stochastic systems. Brian is currently investigating the use of risk management and stochastic optimization techniques for prognostics and prognostics-informed decision making in robotic and aviation applications. From 2011 to 2013 he performed joint research with the Prognostic Center of Excellence at NASA Ames under the NASA graduate student research fellowship. He is currently working as a research engineer for Stinger Ghaffarian Technologies and is conducting joint research with the intelligent systems division at NASA Ames.

Matthew Daigle received the B.S. degree in Computer Science and Computer and Systems Engineering from Rensselaer Polytechnic Institute, Troy, NY, in 2004, and the M.S. and Ph.D. degrees in Computer Science from Vanderbilt University, Nashville, TN, in 2006 and 2008, respectively. From September 2004 to May 2008, he was a Graduate Research Assistant with the Institute for Software Integrated Systems and Department of Electrical Engineering and Computer Science, Vanderbilt University, Nashville, TN. From June 2008 to December 2011, he was an Associate Scientist with the University of California, Santa Cruz, at NASA Ames Research Center. Since January 2012, he has been with NASA Ames Research Center as a Research Computer Scientist. His current research interests include physics-based modeling, model-based diagnosis and prognosis, simulation, and hybrid systems.

George Gorospe received the B.E. degree in Mechanical Engineering from the University of New Mexico, Albuquerque, New Mexico, USA, in 2012. Since October 2012, he has been a research engineer at NASA Ames Research Center. In May 2013 he joined Stinger Ghaffarian Technologies and the Prognostic Center of Excellence at NASA Ames Research Center. His current research interests include space mission design, systems engineering, and autonomous mobile robot control and control systems design.